Morphological factors associated with giant vacuoles with I-pores in Schlemm's canal endothelial cells of human eyes: a serial block-face scanning electron microscopy study

David L. Swain[1,2], **Thuy Duong Le**[1], **Senila Yasmin**[1], **Beatriz Fernandes**[1], **Ganimete Lamaj**[1], **Indira Dasgupta**[1], **Yanyun Gao**[1], **Haiyan Gong**[1,2]

[1]Department of Ophthalmology, Boston University School of Medicine, Boston, MA, USA

[2]Department of Anatomy and Neurobiology, Boston University School of Medicine, Boston, MA, USA

Abstract

Increased intraocular pressure (IOP) is the main risk factor for primary open-angle glaucoma and results from impaired drainage of aqueous humor (AH) through the trabecular outflow pathway. AH must pass the inner wall (IW) endothelium of Schlemm's canal (SC), which is a monolayer held together by tight junctions, to exit the eye. One route across the IW is through giant vacuoles (GVs) with their basal openings and intracellular pores (I-pores). AH drainage through the trabecular outflow pathway is segmental. Whether more GVs with both basal openings and I-pores are present in the active flow areas and factors that may influence formation of GVs with I-pores have not been fully elucidated due to limitations in imaging methods. In this study, we applied a relatively new technique, serial block-face scanning electron microscopy (SBF-SEM) to investigate morphological factors associated with GVs with I-pores in different flow areas. Two normal human donor eyes were perfused at 15 mmHg with fluorescent tracers to label the outflow pattern followed by perfusion-fixation. Six radial wedges of trabecular meshwork including SC (2 each from high-, low-, and non-flow areas) were imaged using SBF-SEM (total: 9,802 images). Total GVs, I-pores, basal openings, and four types of GVs were identified. Percentages of GVs with I-pores and basal openings and number of I-pores/GV were determined. Overall, 14.4% (477/3302) of GVs had I-pores. Overall percentage of GVs with both I-pores and basal openings was higher in high- (15.7%), than low- (12.6%) or non-flow (7.3%) areas. Of GVs with I-pores, 83.2% had a single I-pore; 16.8% had multiple I-pores (range: 2-6). Additionally, 180 GVs (90 with I-pores and 90 without I-pores) were randomly selected, manually segmented, and three-dimensionally (3D) reconstructed to determine size, shape, and thickness of the cellular lining. Size of GVs (including median volume, surface area, and maximal cross-sectional area) with I-pores ($n = 90$) was significantly larger than GVs without I-pores ($n = 90$) using 3D-reconstructed

GVs (P 0.01). Most I-pores (73.3%; 66/90) were located on or close to GV's maximal cross-sectional area with significant thinning of the cellular lining. Our results suggest that larger size and thinner cellular lining of GVs may contribute to formation of GVs with I-pores. More GVs with I-pores and basal openings were observed in high-flow areas, suggesting these GVs do provide a channel through which AH passes into SC and that increasing this type of GV may be a potential strategy to increase aqueous outflow for glaucoma treatment.

Keywords

human eye anatomy; Schlemm's canal endothelium; giant vacuoles; pores; segmental aqueous outflow; serial block-face scanning electron microscopy; 3D electron microscopy

1. INTRODUCTION

Primary open-angle glaucoma (POAG) is an optic neuropathy and one of the leading causes of irreversible blindness worldwide (Quigley, 1995). A primary risk factor for POAG is elevated intraocular pressure (IOP), due to an imbalance between aqueous humor (AH) production and drainage (AGIS Investigators, 2000). The majority of the resistance to drainage, or outflow, is believed to reside in the juxtacanalicular connective tissue (JCT) and to be modulated by the inner wall (IW) endothelium of Schlemm's canal (SC) (Grant, 1958, 1963; Johnson et al., 1992; Maepea and Bill, 1989, 1992; Overby et al., 2009; Vahabikashi et al., 2019). However, the mechanisms that regulate outflow resistance remain unclear.

From the anterior chamber, the majority of AH drains through the trabecular meshwork (TM) to the JCT (Gong and Swain, 2020; Johnson and Erickson, 2000). From the JCT, AH must cross the IW endothelium of SC, which is a monolayer held together by tight junctions (Bhatt et al., 1995; Raviola and Raviola, 1981). There are two mechanisms by which AH crosses the IW: 1) between adjacent IW cells through intercellular pores (B-pores), or 2) through intracellular pores (I-pores) in individual IW cells either associated with a giant vacuole (GV) or not (Ethier et al., 1998; Inomata et al., 1972). This study focuses on GVs and their associated I-pores.

GVs are AH-filled outpouchings, which appear to form due to the pressure drop between anterior chamber and episcleral veins (Grierson and Lee, 1975; Johnstone and Grant, 1973; Tripathi, 1972). The proposed mechanism by which GVs form is through AH pressing on the basal side of an IW endothelial cell causing an invagination known as a basal opening (Tripathi, 1971). I-pores are hypothesized to form in the cellular lining of the GV once the GV size increases and the cell stretches (Braakman et al., 2014; Tripathi, 1972). I-pores allow AH to exit the GVs into the lumen of SC directly from the JCT and after the basal opening has closed (Johnson and Erickson, 2000). GVs with both basal opening and luminal I-pore are thought to provide a channel through which AH may freely pass into SC from the JCT. A recent study investigating normal and glaucomatous donor eyes found similar GV cross-sectional area and density despite a lower flow rate in the POAG eyes due to their higher flow resistance (Vahabikashi et al., 2019). However, two previous scanning electron microscopy (SEM) studies have shown a decrease in the number of pores in eyes with POAG (Allingham et al., 1992; Johnson et al., 2002). It is unknown whether there is a

decrease in the number GVs with I-pores and/or basal openings in POAG and what factors may promote GV and I-pore formation.

Outflow around the circumference of the eye is non-uniform, or segmental, based on observations of fluorescent tracers or fluorescein dye perfused into enucleated eyes (Cha et al., 2016; Huang et al., 2017; Huang et al., 2018; Lu et al., 2008; Lu et al., 2011; Vranka et al., 2015; Yang et al., 2013). These studies suggest that only a fraction of the outflow pathway is actively allowing outflow at any given time. Morphological (Yang et al., 2013) and molecular (Vranka et al., 2015; Vranka et al., 2018) differences have been found between areas of active and inactive flow, or flow-type areas (based on the amount of fluorescent tracer accumulation). One SEM study found increased fluorescent tracer accumulation with increased total pore (both I- and B-pores) density along the IW of SC; however this association was not found with I-pore density alone (Braakman et al., 2015). Another study found no differences in number and cross-sectional area of GVs between active and inactive areas; however, this study, at the light microscopic level, was unable to examine I-pores or basal openings of the GVs (Vahabikashi et al., 2019). No previous studies have investigated the differences in GV volume or density of GVs with I-pores and/or basal openings between different flow-type areas. If GVs with basal openings and I-pores provide a pathway for AH to cross the IW of SC, it may be possible that more of these GVs could be present in high-flow areas compared to low- or non-flow areas.

Previous SEM studies reported that approximately 13-29% of the IW cell bulges have pores in monkey eyes (Bill, 1970; Lee and Grierson, 1975a; Segawa, 1973). When examining the IW of SC, traditional SEM cannot fully distinguish endothelial cell nuclei from GVs among the bulges observed. Transmission electron microscopy can distinguish between GVs and nuclei. However, a large amount of serial thin sections would be required to examine accurately the percentage of GVs with I-pores and basal openings, GV shapes, and volumes, and this is difficult to acquire to study a large number of GVs. With the development of serial block-face scanning electron microscopy (SBF-SEM), thousands of serial cross-sectional images can be acquired, and structures of the outflow pathway can be reconstructed in 3-dimensions (3D). While this method is labor-intensive, it provides an extremely in-depth view of a small sample area. Using SBF-SEM, we previously investigated the role of cellular connectivity between IW endothelial cells of SC and JCT by comparing a small sample of 3D-reconstructed IW endothelial cells and their GVs between immersion- and perfusion-fixed eyes (Lai et al., 2019). We also found that the majority of the pores in the IW are I-pores (Le et al., 2019), consistent with previous studies (Ethier et al., 1998; Johnson et al., 2002). However, differences in GV volumes and types (based on presence of I-pores and/or basal openings) between different flow-type areas at the same pressure have not yet been investigated using SBF-SEM.

In this study, we used SBF-SEM to examine four types of GVs in different flow-type areas in normal human donor eyes perfusion-fixed at 15 mmHg. The goals of this study were to test our hypotheses that: 1) there is a greater percentage of GVs with basal openings and I-pores in high flow areas than low- or non-flow areas; and 2) GVs with I-pores and/or basal openings are larger than those without I-pores. We examined factors that may contribute to

the formation of GVs with I-pores and/or basal openings including flow-type area, GV size, shape, basal openings, and thickness of the cellular lining of the GVs.

2. MATERIALS AND METHODS

2.1 Human Donor Eyes

Two eyes from two donors (Eye 1: 32-years-old; Eye 2: 80-years-old) without any known history of ocular diseases were obtained from the Miracles in Sight Eye Bank (Winston-Salem, NC, USA) within 24-hours postmortem. Eyes were confirmed to be grossly normal under a dissecting microscope and were used in accordance with the guidelines regarding use of human subjects and tissues as outlined in the Declaration of Helsinki.

2.2 Ocular Perfusion and Fixation

The perfusion procedure has been described in detail previously (Scott et al., 2009). Briefly, both eyes were perfused using pressure-controlled hydraulic pumps with Dulbecco's phosphate-buffered saline (pH 7.3; Invitrogen, Grand Island, NY, USA) with 5.5 mM D-glucose (collectively referred as GPBS) for 30 minutes to establish a stable baseline facility at constant pressure of 15 mmHg (Eye 1: 0.263 μl/min/mmHg; Eye 2: 0.318). Eyes were then exchanged and perfused with a fixed volume (200 μL; 1:1000 dilution in GPBS) of red fluorescent tracers (size: 200 nm; Catalog number: F8810; Thermo Fisher Scientific, Waltham, MA, USA), followed by perfusion-fixation with modified Karnovsky's fixative (2.5% glutaraldehyde and 2% paraformaldehyde in 0.1-M sodium phosphate buffer; pH = 7.3) for 30 min. A small cut (~5 mm) was gently made along the equator, and eyes were then immersed in the same fixative overnight.

2.3 Global Imaging and Ocular Dissection

To visualize the segmental outflow pattern along the entire limbus, global imaging was performed, as described previously (Cha et al., 2016). Briefly, globes were hemisected into anterior and posterior segments. The iris, ciliary body, cornea (10 mm trephine), vitreous, and excess conjunctiva were removed. Anterior segments were imaged *en face* on both TM and episcleral surfaces with a 300 mm lens on a 4000 MP VersaDock imaging system (Bio-Rad Laboratories, Hercules, CA, USA) using Quantity One (Bio-Rad) software (fixed exposure time: 5 s) (Fig 1).

Guided by global images, tissue wedges (2 x 2 x 2 mm) of the TM, including SC were dissected from each of the following flow-type areas: high-, low-, and non-flow (Fig 1) from each eye (total: 6 wedges). Flow-type areas were determined based on the amount of fluorescence observed on the TM and episcleral surfaces. High-flow areas had bright fluorescence on both posterior (trabecular meshwork) and anterior (episcleral veins) sides. Low-flow areas had intermediate fluorescence on both sides. Non-flow areas had no visible fluorescence on either side. Number of tracers was estimated for each block, as described below in morphometric analysis.

2.4   Serial Block-Face Scanning Electron Microscopy

Tissue wedges were sent to Cleveland Clinic (Cleveland, OH) for processing. A SBF-SEM technician at Cleveland Clinic processed and embedded the tissue into Epon blocks using a previously described method (Deerinck et al., 2010). Briefly, tissues were post-fixed with OsO4/K ferrocyanide and thiocarbohydrazide and *en-bloc* stained with uranyl acetate and lead aspartate. Tissues were dehydrated with a series of ethanol dilutions and embedded in Epon resin. The regions of interest (including SC and TM) in each block were imaged using a Zeiss Sigma VP serial block-face scanning electron microscope equipped with a Gatan 3View (Gatan, Inc., Pleasanton, CA, USA) in-chamber ultramicrotome stage and low-kV backscattered electron detectors that were optimized for 3View systems. After each image was taken of the block face, the automated ultramicrotome cut a section, and then another image was taken of the block face until the entire block was cut through. Pixel size was 0.0101 μm x 0.0101 μm, and section thickness was 0.13 μm. Field size was 141 μm x 60 to 71 μm. An example of the full imaging field for each electron micrograph is shown in Fig 2A. Images were compiled, aligned, and sent to Boston University School of Medicine for analysis.

2.5   Morphometric Analysis and 3D Reconstruction

2.5.1   Whole-Block Analysis—Image sets were visualized in Reconstruct (Fiala, 2005). A total of 9,802 images were screened from six blocks of tissue. Flow-type areas were confirmed on SBF-SEM images by labeling the fluorescent tracers within the JCT throughout each block every 50 sections using the stamp tool in Reconstruct. An example of tracers on an SBF-SEM image is shown in Fig 2B. Mean number of tracers per section was determined for each block (Eye 1: high-flow: 194 tracers/section, low-flow: 57, non-flow: 31; Eye 2: high-flow: 477, low-flow: 161, non-flow: 40).

All GVs were marked throughout each block on each section in which they appeared and counted. GVs that were completely within the imaging field ($n = 3302$) were assessed for the presence of luminal I-pores and basal openings by at least two individual investigators (DLS, TDL, SY, BF). I-pores were identified as openings in the cellular lining surrounding the GVs that had smooth borders with clear separation. Openings in the cellular lining that appeared rough or were in line with knife marks from the sectioning process were excluded. GVs were typed according to previous studies: Type I: no basal opening or I-pore; Type II: basal opening, no I-pore; Type III: I-pore, no basal opening; and Type IV: both basal opening and I-pore (Fig 3) (Grierson and Lee, 1978; Koudouna et al., 2019). Percentages of each type of GV were determined by the number of each type of GV divided by the total number of GVs within the imaging field for each block, by flow-type area, and overall. The total percentage of GVs with I-pores was determined by the number of GVs observed with I-pores divided by the total number of GVs within the imaging field. Of the GVs with I-pores, the percentages with a single I-pore or multiple I-pores were determined. The size of GVs was estimated by median span (number of sections in which a GV appears) and compared between the GVs with or without I-pores overall and in each flow-type area, and among GV types.

For the two eyes in our study, we estimated GV density for each block by two methods: 1) number of GVs/ number of IW cell nuclei; and 2) number of GVs/ IW surface area. Nuclei of IW endothelial cells were marked and counted throughout all blocks. For this analysis, GVs and nuclei that were partially out of the imaging field on the right-hand side or at the end of the block were excluded. Conversely, GVs and nuclei were included if they were partially out of the imaging field on the left-hand side or at the beginning of the block. This was done to account for the GVs found across the entire surface area of IW in each block. Subsequently, to estimate the density of GVs with I-pores, the GV densities were multiplied by the percentage of GVs with I-pores (as determined above).

The IW of SC surface area for each block was estimated as follows: SA = width of IW_1(total sections/3)(0.13 μm) + width of IW_2(total sections/3)(0.13 μm) + width of IW_3(total sections/3)(0.13 μm), where width of IW measured in Reconstruct by drawing a line along the inner wall of SC in each image. Three measurements were made evenly spaced apart throughout each block. Each measurement was taken to represent the width for one-third of the sections and was therefore multiplied by (total sections/3). Three measurements were taken, because each block was ~1600 sections, which represented a length of ~212 μm of IW (calculated as mean number of sections for six blocks multiplied by section thickness: 1634 x 0.13 μm).

2.5.2   Analysis of 180 3D-Reconstructed GVs—To investigate size, shapes, and thickness of the cellular lining of the GVs, a subset of GVs ($n = 180$) that were completely within the imaging field with I-pores ($n = 90$) and without I-pores ($n = 90$) were traced manually and reconstructed in 3D (Fig 4). An equal number of GVs with ($n = 15$) and without ($n = 15$) I-pores were selected from each flow-type area (high-, low-, and non-flow) from each eye. The following process was used to select randomly 180 GVs to reconstruct. When all GVs were labeled during whole-block analysis, they were assigned a number identity. A random number generator was used to select GVs using those identities. If the random number generator produced a number for a GV that was partially out of the imaging field, another number was generated. GVs were not included if their volumes were not equal to or greater than 1 $μm^3$ to differentiate between GVs and pinocytotic vesicles (Grierson and Lee, 1975, 1977; Grierson et al., 1978).

GV volumes were calculated using the Volume tool in Reconstruct. Volumes were compared in the following ways: 1) between GVs with and without I-pores; 2) between GVs with a single I-pore and with multiple I-pores; 3) between GV types I-IV. GV surface area was determined with the Surface Area tool in Reconstruct. The maximal cross-sectional area (CSA) of the GV was determined using the Area tool when tracing the GVs manually.

Shapes of GVs were classified as round or collapsed based on their 3D reconstructions (Supplemental Video S1). GVs were categorized as collapsed if: 1) at least 50% of the GV's luminal aspect was concave and 2) the point of furthest indentation was below the horizontal axis of the GV parallel to the IW. All other GVs, even with minor indentations, were classified as round. Percentages of round and collapsed GVs with and without I-pores were compared. Volumes were compared between round and collapsed GVs.

Thickness of the cellular lining of the GVs was measured on the border of each GV in two places on the section with the maximal CSA of the GV: 1) *top*, in line with the central axis of the GV perpendicular to the IW; and 2) *side*, 90° counter-clockwise from the top measurement (Fig 5A). These measurements were averaged and compared to similar top and side measurements taken on a section "away" from the maximal CSA section. The "away" section was determined by the following formula: [(last section in which GV appears) - (section with maximal CSA)]*(0.67). For example, if a GV last appeared in section 200 and its maximal CSA was section 150, the away measurement was done on section 184. This accounted for GVs of different sizes and ensured the away measurements were performed on sections with significantly smaller CSAs than sections with the maximal CSAs but not too close to the end of the GV. The thickness of the cellular lining of the GVs was also measured on the sections before and after the largest I-pore appears ($n = 90$) in the region of the lining near the I-pore, or peri-pore region, and 90° counter-clockwise away from the peri-pore area (Fig 5B). If a nucleus or the base of the cell was present 90° counter-clockwise away from the peri-pore measurement, the away measurement was taken clockwise.

The proximity of I-pores to the maximal CSA section of the GV was determined by the following calculation: (number of sections from maximal CSA of the GV to the I-pore) / (number of sections from the maximal CSA to the end of the GV). This was done to account for GVs of different sizes. For example, if the number of sections from maximal CSA to the I-pore was 5 sections and the number of sections from the maximal CSA to the end of the GV was 50 sections, the I-pore was within 10% (5/50) of sections from maximal CSA. If a GV had multiple I-pores, the I-pore closest to the maximal CSA section was used.

2.6 Statistical Methods

All data are listed as median (interquartile range: quartile 1 – quartile 3) or mean ± SEM. All statistical analyses were performed using R statistical computing package (v3.5.1; R Foundation for Statistical Computing, Vienna, Austria). Chi-square tests were used to compare percentages of GVs with single and multiple I-pores between flow-type areas, proportions with basal openings or not, and to compare distributions of GV types I-IV in different flow-type areas. Kolmogorov-Smirnov (KS) tests were used to test for normality of the data distributions. KS tests for GV span, volumes, surface area, maximal CSA reported non-normal distributions (all P 0.01); for this reason, non-parametric Kruskal-Wallis tests with post-hoc pairwise Wilcoxon-rank sum tests were used to test for statistical significance. KS test for thickness of the cellular lining of the GVs reported normal distributions ($P >$ 0.05); therefore, paired Student's *t*-tests were used to compare measurements of the thickness of the cellular lining of the GVs on the sections with maximal CSA and the sections away from the maximal CSA and between the peri-pore region and 90° away on the same sections.

3. RESULTS

3.1 Whole-Block Analysis

Overall, 3,450 GVs, 582 I-pores, and 543 IW nuclei were observed over an inner wall surface area of 0.166 mm^2 in 9,802 serial electron micrographs. Table 1 summarizes the

number of images, I-pores, nuclei, and IW surface area for each flow-type area for each eye. Table 2 summarizes the number of GVs observed over the entire surface area, the number of GVs that were completely within the imaging field, the number of GVs with I-pores, and percentage of GVs with I-pores.

3.1.1   Analysis of GVs with I-pores and/or basal openings, GV types I-IV—Of the 3450 GVs observed, 3302 GVs were completely within the imaging field and used for the following analyses. Overall, 477 / 3302 (14.4%) GVs had I-pores. The following trend was observed in both eyes: the percentage of GVs with I-pores was highest in high-flow, then low-flow, then non-flow (Table 2). The overall percentages of GVs with I-pores was significantly different among flow-type areas (Chi-square test for independence, $\chi^2 = 45.40$, P 0.01). Of GVs with I-pores, 397/477 (83.2%) only had a single I-pore, and 80/477 (16.8%) had more than one I-pore (Examples in Figs 6 and 7): 63 (13.2%) had two I-pores, 13 GVs (2.7%) had three I-pores, 2 GVs (0.4%) had four I-pores, and only 2 GVs of the 477 GVs observed with I-pores had six I-pores (0.4%) (Supplemental Fig S1). The proportions of GVs with a single I-pore to GVs with multiple I-pores were similar among flow-type areas (Chi-square test for independence, $\chi^2 = 0.7216$, $P = 0.70$); however, non-flow area had a range of 1-3 I-pores / GV, whereas high- and low-flow both had ranges of 1-6 I-pores / GV (Supplemental Fig S1).

Of the 3302 GVs completely within the imaging field, 2,296 GVs (69.5%) had basal openings, and 1006 GVs (30.5%) did not have a basal opening. Of the 477 GVs with I-pores, 392 GVs (82.2%) also had a basal opening. Of the 2825 GVs without I-pores, 1904 GVs (67.4%) had a basal opening.

GVs were typed according to previous studies (Grierson and Lee, 1978; Koudouna et al., 2019), and examples are shown in Fig 3. Of 3302 GVs, there were 27.9% Type I (no basal opening or I-pore), 57.7% Type II (basal opening, no I-pore), 2.5% Type III (I-pore, no basal opening), and 11.8% Type IV GVs (both basal opening and I-pore) (Table 3). A significant difference was found in the proportions of GV types I-IV among high-, low-, and non-flow areas (Chi-square test of independence, $\chi^2 = 63.32$, P 0.01). Specifically, the overall proportion of Type I GVs was significantly less in high- (23.4%) and low-flow (26.7%) areas compared to non-flow areas (33.4%) ($\chi^2 = 30.12$, P 0.01; and $\chi^2 = 9.70$, P 0.01, respectively). The proportion of Type IV GVs was significantly higher in high- (15.7%) and low-flow areas (12.6%) compared to non-flow (7.3%) areas ($\chi^2 = 42.55$, $P < 0.01$; and $\chi^2 = 16.06$, P 0.01, respectively) (Table 3). Tracers were observed in the pathway of Type IV GVs: from the JCT, inside the GVs themselves, and in the lumen of SC near I-pores in high-flow areas (Fig 8).

3.1.2   Span of giant vacuoles—Overall, GVs spanned a median of 31 sections (range: 9-333, $n = 3302$). The median span of GVs with I-pores (61 sections, $n = 477$) was significantly larger than GVs without I-pores (27 sections, $n = 2825$; Wilcoxon rank-sum test, P 0.01, Fig 9A). When analyzed by flow-type area, GVs with I-pores were significantly larger than GVs without I-pores in high-, low-, and non-flow areas (all P 0.01; Fig 9B–D). Median span of GVs with multiple pores (80 sections) was significantly larger than GVs with a single pore (57; P 0.01; Figure 9E). Median span of Types I, II, III,

and IV GVs were 22, 31, 46, and 65 sections, respectively, which varied significantly (Kruskal-Wallis test, P 0.01; Fig 9F). Specifically, median span of Type IV GVs (with both basal opening and I-pore) were significantly larger than Types I, II, and III (all P 0.01). Median span of Type I GVs (no basal opening or I-pore) was significantly smaller than Types II, III, and IV (all P 0.01).

3.1.3   Density of giant vacuoles with pores—Density of GVs with I-pores / IW nucleus, and density of GVs with I-pores / IW area for both eyes are summarized in Table 4. The following trends were observed in the two eyes investigated. In Eye 1, density of GVs with I-pores / nucleus and / IW area were highest in high-flow, then low-flow, then non-flow. In Eye 2, density of GVs with I-pores / IW area was highest in high-flow, then non-flow, then low-flow. Although Eye 2 non-flow area had only a small percentage of GVs with I-pores, the density of GVs with I-pores was still greater than low-flow area. Overall, the trend observed in the two eyes in our study was that high-flow area had higher density of GVs with I-pores, compared to low- and non-flow areas.

3.2   Analysis of 180 3D-Reconstructed Giant Vacuoles

The volume, surface area, shape of GVs, and the thickness of cellular lining of the GVs were analyzed in 180 3D-reconstructed GVs, including 90 GVs with I-pores and 90 GVs without I-pores.

3.2.1   Giant vacuole size

3.2.1.1   Giant vacuole volume: Using all 3D-reconstructed GVs, median volume of GVs with I-pores was significantly larger (116.93 μm^3, $n = 90$) than GVs without I-pores (54.82 μm^3, $n = 90$; Wilcoxon-rank sum test, P 0.01; Fig 10A).

When analyzed by flow-type area, in high-flow area, median volume of GVs with I-pores (172.39 μm^3, $n = 30$) was not quite statistically larger than GVs without I-pores (55.12 μm^3, $n = 30$; Wilcoxon-rank sum test, $P = 0.07$; Fig 10B). In low- and non-flow areas, median volume of GVs with I-pores (127.00 μm^3, 113.91 μm^3) was significantly larger than GVs without I-pores (37.57 μm^3 and 58.34 μm^3; $P = 0.01$ and $P = 0.03$, respectively) (Fig 10C–D). There were no significant differences in median volumes of GVs with I-pores (Kruskal-Wallis test, H = 0.2591, $P = 0.88$) or GVs without I-pores (H = 0.0495, $P = 0.98$) among flow-type areas. Of all GVs with I-pores, median volume of GVs with multiple I-pores (212.59 μm^3, $n = 33$) was significantly larger than GVs with a single I-pore (75.80 μm^3, $n = 57$; Wilcoxon-rank sum test, P 0.01; Fig 10E).

Median GV volumes varied significantly among the four types of GVs (Kruskal-Wallis test, P 0.01; Fig 9F). Median volume of Type I (no basal opening or I-pore), Type II (with basal opening, no I-pore), Type III (with I-pore, no basal opening), and Type IV (with both basal opening and I-pore), were 20.78 μm^3, 79.65 μm^3, 45.78 μm^3, 119.72 μm^3, respectively. Median volume of Type II GVs was significantly larger than Type I (Wilcoxon rank-sum test, $P = 0.01$). Median volume of Type IV GVs was significantly larger than Types I, II, and III (P 0.01 compared to Types I and II; $P = 0.03$ compared to Type III; Fig 10F).

3.2.1.2   Giant vacuole surface area: Median surface area of reconstructed GVs with I-pores (135.62 μm^2, n = 90) was significantly larger compared to those without I-pores (78.16 μm^2, n = 90; Wilcoxon rank-sum test, P 0.01; Supplemental Figure S2A). Median surface area of reconstructed GVs with multiple I-pores (201.82 μm^2, n = 33) was significantly larger than GVs with a single pore (93.90 μm^2, n = 57; P 0.01; Supplemental Figure S2B). Median surface area of Type I, II, III, and IV GVs was 36.98 μm^2 (n = 19), 93.86 μm^2 (n = 71), 58.01 μm^2 (n = 11), and 150.56 μm^2 (n = 79), respectively. Median surface area of reconstructed GVs varied significantly among types I-IV (Kruskal-Wallis test, P 0.01). Specifically, Type IV GVs were significantly larger than Types I and II (both P < 0.01) (Supplemental Figure S2C).

3.2.1.3   Maximal cross-sectional area of giant vacuoles: Median maximal CSA of reconstructed GVs with I-pores (21.29 μm^2, n = 90) was significantly larger compared to GVs without I-pores (13.66 μm^2, n = 90; Wilcoxon rank-sum test, P 0.01) (Supplemental Figure S2D). Median maximal CSA of reconstructed GVs with multiple I-pores (25.87 μm^2, n = 33) was significantly larger than GVs with a single I-pore (17.49 μm^2, n = 57; P = 0.02; Supplemental Figure S2E). Median maximal CSA of Type I, II, III, and IV GVS was 8.56 μm^2 (n = 19), 15.96 μm^2 (n = 71), 16.11 μm^2 (n = 11), and 22.71 μm^2 (n = 79), respectively. Median maximal CSA varied significantly among types I-IV (Kruskal-Wallis test, P 0.01). Specifically, GV Type IV maximal CSA was significantly larger than Types I and II (P 0.01 and P = 0.04, respectively) (Supplemental Figure S2F).

3.2.2   Giant vacuole shapes—Following 3D reconstruction, each GV (n = 180) was classified by shape as round or collapsed, according to our previous study (Lai et al., 2019). Examples of the two shape classes are shown in Supplemental Fig S3A–D and Supplemental Video S1. We found that 163/180 (90.6%) of reconstructed GVs were round, compared to 17/180 (9.4%) that were collapsed. We found similar percentages of GVs with I-pores in round (49.7%) and collapsed (52.9%) GVs (Supplemental Fig S3E). Median volume of round GVs (85.15 μm^3; n = 163) was not significantly smaller than collapsed GVs (139.13 μm^3; n = 17; Wilcoxon rank-sum test, P = 0.15; Supplemental Fig S3F). The percentage of GVs with basal openings that were collapsed (8.00%, 12/150) was not significantly lower compared to the percentage of GVs without basal openings that were collapsed (16.67%, 5/30; Chi-square test for independence, χ^2 = 2.19, P = 0.14).

3.2.3   Thickness of the cellular lining of the GVs—Mean thickness of the cellular lining of the GVs on the sections with maximal GV CSA was significantly thinner (0.288 ± 0.014 μm; n =180), compared to mean thickness on sections away from maximal CSA (0.326 ± 0.016 μm; n = 180; paired Student's t-test, P = 0.03; Fig 11A). Mean thickness of Types II and IV GVs (0.253 ± 0.016; 0.278 ± 0.015, respectively) were significantly thinner than Type I GVs (0.433 ± 0.083; unpaired Student's t-tests, both P 0.01) on the sections with the maximal GV CSA. Mean thickness was significantly thinner in the peri-pore area (0.176 ± 0.011 μm; n = 90), compared to   90° away on the same section (0.324 ± 0.019 μm; n =90; paired Student's t-test, P < 0.01; Fig 11B).

3.2.4 Proximity of I-pores to maximal cross-sectional area of GV—For the 3D-reconstructed GVs with I-pores ($n = 90$), we found that 12/90 (13.3%) of I-pores were present in the section with the maximal CSA of the GV (*red points* in Fig 12). 38/90 (42.2%) of I-pores were either on or within the first 25% of sections and 66/90 (73.3%) were present within the first 50% of sections from maximal CSA to end of GV (Fig 12). Overall, most I-pores (73.3%) were closer to the section with maximal CSA than to the end of the GV (Chi-square test goodness of fit, $\chi^2 = 19.60$, P 0.01).

4. DISCUSSION

In this study, we examined 3302 GVs in the inner wall endothelial cells of SC of two perfused normal human eyes in depth by analyzing over 9,800 SBF-SEM images and 180 3D reconstructed GVs. Specifically, we determined the percentage of GVs with I-pores and basal openings in different flow-type areas and investigated factors associated with GVs with I-pores in SC endothelial cells, including GV size, shapes, and thickness of the cellular lining of the GVs. Our main findings were: 1) significantly more GVs with both I-pores and basal openings (Type IV) were found in high- and low-flow compared to non-flow areas; 2) GVs with I-pores were significantly larger (span, volume, surface area) than those without I-pores; 3) 16.8% of GVs with I-pores had multiple pores, and GVs with multiple pores were larger than GVs with a single pore; and 4) thinner cellular lining of the GVs was found near maximal CSA, in GVs with both basal opening and I-pore, and near I-pores.

In this study, we found that 14.4% GVs overall had I-pores, which was similar to previous studies reporting 14.6% of GVs had pores in human eyes (Lai et al., 2019), and 13–29% in monkey eyes (Bill, 1970; Lee and Grierson, 1975a; Segawa, 1973). Additionally, we found a higher percentage of GVs with both I-pores and basal openings (Type IV) and a higher density of GVs with pores per nucleus or unit IW area in high-flow areas compared to low- and non-flow areas in our two eyes. Our results are consistent with our hypothesis that there are more GVs with I-pores and basal openings in high-flow areas than low- or non-flow areas. We observed tracers in the JCT underneath the basal openings of Type IV GVs, inside the GVs themselves, and in the lumen of SC near I-pores in these GVs (Fig 8). Although the time-course of when the tracer was deposited in the JCT in relation to the GVs' lifespans cannot be determined from our static imaging, the observation that the tracers co-localize with Type IV GVs suggests that these GVs allow AH to cross into SC. Overall, our findings suggest that GVs with both I-pores and basal openings are an indicator of greater flow across the IW of SC and that increasing the number of this type of GV could be a potential new strategy to increase aqueous outflow and decrease IOP in glaucoma treatment.

By examining the factors associated with GVs with I-pores, we found that GVs with I-pores had a larger median span, volume, surface area, and maximal CSA than those without I-pores. This finding supports our hypothesis that increasing size of a GV is a factor that may influence I-pore formation, which could be triggered through biomechanical strain (Braakman et al., 2014; Zhou et al., 2012). By examining the thickness of the cellular lining of the GVs, we found: 1) thickness was significantly thinner at the maximal CSA section, compared to sections away from maximal CSA; 2) Type IV GVs had significantly thinner cellular lining compared to Type I GVs; 3) thickness of the cellular lining became

significantly thinner near I-pores compared to 90° away from the I-pore on the same sections. These findings suggest that I-pores may form due to thinning of the cellular lining of the GVs when GVs become larger. We observed that most of the I-pores on 3D-reconstructed GVs (73.3%) were closer to the section with maximal CSA, where the cellular lining was thinner. This suggests that I-pores may form due to cell stretching as the GV expands and increases in size. Further studies of the cytoskeleton of IW endothelial cells with GVs is warranted to further elucidate this relationship.

A recent study used SBF-SEM to investigate the regional variation in the ultrastructure of the JCT and IW in one block of tissue of one human eye (Koudouna et al., 2019). The authors examined only 40 GVs and found an uneven distribution of GV types I-IV, which they suggested supports the existence of segmental outflow areas (Koudouna et al., 2019). However, this study did not perfuse fluorescent tracers to localize areas of high-, low-, and non-flow, and the eye was immersion-fixed. In our current study, we also observed a significant difference in the proportions of GV types I-IV in three flow-types areas (Table 3), using tracer labelling and perfusion-fixation. We found that there were fewer Type I (no basal opening or luminal I-pore) and more Type IV (both basal opening and luminal I-pore) in high- and low-flow compared to non-flow areas. These findings may suggest that more flow (areas with more tracers) correlate with more GVs with both basal openings and I-pores, which form a channel through which AH may pass from JCT into the lumen of SC. Since our study only investigated two eyes, further studies are required to confirm these findings in a larger number of eyes.

SBF-SEM allowed for in-depth study of the GVs in the IW of SC including density, size, and shape. With this method, we found larger values for the density of GVs per IW nucleus compared to previous studies, which may be because we were able to find many smaller GVs that were not detected using previous methods, even though our criteria for inclusion of GVs were similar (Grierson and Lee, 1978; Lee and Grierson, 1975a). We also quantified for the first time that of the GVs with pores, 16.8% of them have more than one I-pore in human eyes. A previous SEM had observed two openings on IW cell bulges in monkey eyes but stated that three or four openings were very rare (Lee and Grierson, 1975b). Because we could scan through each GV with a section thickness of 0.13 μm, we could quantify the number of GVs with multiple I-pores, which has not been done before. Additionally, we also found that GVs with multiple I-pores are larger (span, volume, surface area, and maximal CSA) than GVs with a single I-pore (P 0.01). Our findings suggest that larger GV size is associated with the presence of multiple I-pores.

Our findings also suggest that the vacuolation cycle of a GV may be more complicated than previously proposed. The proposed model (Tripathi, 1972) does not include GV Type I (neither basal opening nor luminal I-pore). This type of GV represented 27.9% of the total GVs observed in our current study (Table 3). A previous study using SBF-SEM found similar densities of GVs/cell in immersion-fixed (0 mmHg) and perfusion-fixed (15 mmHg) cells (Lai et al., 2019). We reexamined the 42 GVs from 12 IW cells observed in our previous study of immersion-fixed eyes for basal openings. We found that these GVs were mostly Type I (36/42; 85.71%) and some Type II (6/42; 14.29%). None of these GVs had I-pores. Together, these results suggest that GVs may not disappear all the way but become

very small Type I GVs without basal openings or I-pores, which may be difficult to detect with random transmission electron microscopy sections. Also, Tripathi's model does not describe GV Type III. Our study found only 2.5% of GVs were Type III, suggesting that this stage where the basal opening has closed before closure of the luminal I-pore may occur very rapidly and is not commonly observed.

More than half of the GVs (57.7%) observed were Type II GVs, suggesting either this stage may last for a longer time than other stages or represent two population of GVs during the vacuolation cycle. One population of GVs may increase their size to form I-pores and become Type IV GVs; the other population of GVs may decrease their size and close their basal openings to become Type I GVs. Of all GVs with pores, 82% had basal openings and were Type IV GVs (11.8% of all GVs), which were significantly larger than Type II GVs, which further support that size may be a contributing factor for formation of GVs with I-pores. An advantage of our SBF-SEM method is the ability to scan each GV and quantify these stages of GVs during a moment in time. However, further in-vivo imaging techniques will be needed to determine in what order these stages occur.

While SBF-SEM allowed careful examination of the IW of SC, there were some limitations in this study. SBF-SEM is time-consuming and labor-intensive, so only a small area of SC from each flow-type area per eye could be investigated from a small sample size ($n = 2$ eyes). SBF-SEM is also a static imaging modality, so we cannot determine the time point of pore formation in the lifespan of a GV or the exact order of GV stages and shapes. We cannot determine whether GVs without I-pores had not yet formed an I-pore or an I-pore already closed. Also, the measured morphological parameters in this study may be somewhat magnified, since our perfusion pressure of 15 mmHg represents a higher pressure drop across the IW of SC than physiological pressure *in vivo*, due to absence of episcleral venous pressure in enucleated eyes. Also, we initially classified flow-type areas relatively based on the fluorescent tracer distribution in both TM and episcleral veins visualized during global imaging. When we further quantified the number of tracers on the SBF-SEM images, we found that the areas labeled as low- and non-flow were not uniformly low- and non-flow through the entire length of the block of ~1500 serial images, which may explain some of the similarity in the densities of GVs with I-pores in Eye 2.

In summary, SBF-SEM provided an in-depth method to study GVs in 3D and enabled us to explore some factors that may contribute to formation of GVs with I-pores. We found that larger GV size and thinner cellular lining of the GVs were associated with GVs with I-pores and there was a larger percentage of GVs with I-pores and basal openings (Type IV) in high-flow areas compared to low- and non-flow areas. Our results suggest that increasing the number of GVs with I-pores and basal openings may increase the amount of effective aqueous outflow area and could therefore potentially increase outflow/reduce IOP for glaucoma treatment.

Supplementary Material

Refer to Web version on PubMed Central for supplementary material.

ACKNOWLEDGMENTS

Abbreviations:

AH	aqueous humor
CSA	cross-sectional area
GV	giant vacuole
I-pore	intracellular pore
IOP	intraocular pressure
IW	inner wall
JCT	juxtacanalicular connective tissue
POAG	primary open-angle glaucoma
SBF-SEM	serial block-face scanning electron microscopy
SC	Schlemm's canal
SEM	scanning electron microscopy
TM	trabecular meshwork

REFERENCES

AGIS Investigators, 2000. The Advanced Glaucoma Intervention Study (AGIS): 7. The relationship between control of intraocular pressure and visual field deterioration. Am J Ophthalmol 130, 429–440. [PubMed: 11024415]

Allingham RR, de Kater AW, Ethier CR, Anderson PJ, Hertzmark E, Epstein DL, 1992. The relationship between pore density and outflow facility in human eyes. Invest Ophthalmol Vis Sci 33, 1661–1669. [PubMed: 1559766]

Bhatt K, Gong H, Freddo TF, 1995. Freeze-fracture studies of interendothelial junctions in the angle of the human eye. Invest Ophthalmol Vis Sci 36, 1379–1389. [PubMed: 7775116]

Bill A, 1970. Scanning electron microscopic studies of the canal of Schlemm. Exp Eye Res 10, 214–218. [PubMed: 4991873]

Braakman ST, Pedrigi RM, Read AT, Smith JA, Stamer WD, Ethier CR, Overby DR, 2014. Biomechanical strain as a trigger for pore formation in Schlemm's canal endothelial cells. Exp Eye Res 127, 224–235. [PubMed: 25128579]

Braakman ST, Read AT, Chan DW, Ethier CR, Overby DR, 2015. Colocalization of outflow segmentation and pores along the inner wall of Schlemm's canal. Exp Eye Res 130, 87–96. [PubMed: 25450060]

Cha ED, Xu J, Gong L, Gong H, 2016. Variations in active outflow along the trabecular outflow pathway. Exp Eye Res 146, 354–360. [PubMed: 26775054]

Deerinck TJ, Bushong E, Thor A, Ellisman M, 2010. NCMIR methods for 3D EM: a new protocol for preparation of biological specimens for serial block face scanning electron microscopy. Microscopy, 6–8.

Ethier CR, Coloma FM, Sit AJ, Johnson M, 1998. Two pore types in the inner-wall endothelium of Schlemm's canal. Invest Ophthalmol Vis Sci 39, 2041–2048. [PubMed: 9761282]

Fiala JC, 2005. Reconstruct: a free editor for serial section microscopy. J Microscopy 218, 52–61.

Gong H, Swain DL, 2020. Anatomy of the conventional aqueous outflow pathway, in: Samples JR, Ahmed IIK (Eds.), Current Developments in Glaucoma Surgery and MIGS. Kugler Publications, Amsterdam, The Netherlands, pp. 1–38.

Grant WM, 1958. Further studies on facility of flow through the trabecular meshwork. AMA Arch Ophthalmol 60, 523–533. [PubMed: 13582305]

Grant WM, 1963. Experimental aqueous perfusion in enucleated human eyes. Arch Ophthalmol 69, 783–801. [PubMed: 13949877]

Grierson I, Lee WR, 1975. Pressure-Induced Changes in the Ultrastructure of the Endothelium Lining Schlemm's Canal. Am J Ophthalmol 80, 863–884. [PubMed: 811121]

Grierson I, Lee WR, 1977. Light microscopic quantitation of the endothelial vacuoles in Schlemm's canal. Am J Ophthalmol 84, 234–246. [PubMed: 407798]

Grierson I, Lee WR, 1978. Pressure effects on flow channels in the lining endothelium of Schlemm's canal. A quantitative study by trasmission electron microscopy. Acta Ophthalmol 56, 935–952. [PubMed: 103360]

Grierson I, Lee WR, S A, Howes RC, 1978. Associations between the Cells of the Walls of Schlemm's Canal. Albrecht Von Graefes Arch Klin Exp Ophthalmol 208, 33–47. [PubMed: 103456]

Huang AS, Camp A, Xu BY, Penteado RC, Weinreb RN, 2017. Aqueous Angiography: Aqueous Humor Outflow Imaging in Live Human Subjects. Ophthalmology 124, 1249–1251. [PubMed: 28461013]

Huang AS, Penteado RC, Saha SK, Do JL, Ngai P, Hu Z, Weinreb RN, 2018. Fluorescein aqueous angiography in live normal human eyes. J Glaucoma 27, 957–964. [PubMed: 30095604]

Inomata H, Bill A, Smelser GK, 1972. Aqueous humor pathways through the trabecular meshwork and into Schlemm's canal in the cynomolgus monkey (*Macaca iris*): an electron microscopic study. Am J Ophthalmol 73, 760–789. [PubMed: 4623937]

Johnson M, Chan D, Read AT, Christensen C, Sit A, Ethier CR, 2002. The pore density in the inner wall endothelium of Schlemm's canal of glaucomatous eyes. Invest Ophthalmol Vis Sci 43, 2950–2955. [PubMed: 12202514]

Johnson M, Erickson K, 2000. Mechanisms and routes of aqueous humor drainage, in: Albert DM, Jakobiec FA (Eds.), Principles and Practice of Opthahlmology. W.B. Saunders Company, pp. 2577–2595.

Johnson M, Shapiro A, Ethier CR, Kamm RD, 1992. Modulation of outflow resistance by the pores of the inner wall endothelium. Invest Ophthalmol Vis Sci 33, 1670–1675. [PubMed: 1559767]

Johnstone M, Grant WM, 1973. Pressure-dependent changes in structures of the aqueous outflow system of human and monkey eyes. Am J Ophthalmol 75, 365–383. [PubMed: 4633234]

Koudouna E, Young RD, Overby DR, Ueno M, Kinoshita S, Knupp C, Quantock AJ, 2019. Ultrastructural variability of the juxtacanalicular tissue along the inner wall of Schlemm's canal. Mol Vis 25, 517–526. [PubMed: 31588175]

Lai J, Su Y, Swain DL, Huang D, Getchevski D, Gong H, 2019. The Role of Schlemm's Canal Endothelium Cellular Connectivity in Giant Vacuole Formation: A 3D Electron Microscopy Study. Invest Ophthalmol Vis Sci 60, 1630–1643. [PubMed: 30995299]

Le TD, Swain DL, Lai J, Lam C, Gong H, 2019. Changes in Pore Densities of the Inner Wall Endothelium of Schlemm's Canal with Increasing Pressures Using 3D Serial Block-Face Scanning Electron Microscopy, Association for Research in Vision and Ophthalmology. Invest Ophthalmol Vis Sci, Vancouver, Canada, p. 3182.

Lee WR, Grierson I, 1975a. Pressure effects on the endothelium of the trabecular wall of Schlemm's canal: a study by scanning electron microscopy. Albrecht Von Graefes Arch Klin Exp Ophthalmol 196, 255–265. [PubMed: 813538]

Lee WR, Grierson I, 1975b. Pressure effects on the endothelium of the trabecular wall of Schlemm's canal: a study by scanning electron microscopy. Albrecht Von Graefes Arch Klin Exp Ophthalmol 196, 255–265. [PubMed: 813538]

Lu Z, Overby DR, Scott PA, Freddo TF, Gong H, 2008. The mechanism of increasing outflow facility by rho-kinase inhibition with Y-27632 in bovine eyes. Exp Eye Res 86, 271–281. [PubMed: 18155193]

Lu Z, Zhang Y, Freddo TF, Gong H, 2011. Similar hydrodynamic and morphological changes in the aqueous humor outflow pathway after washout and Y27632 treatment in monkey eyes. Exp Eye Res 93, 397–404. [PubMed: 21669200]

Maepea O, Bill A, 1989. The pressures in the episcleral veins, Schlemm's canal and the trabecular meshwork in monkeys: effects of changes in intraocular pressure. Exp Eye Res 49, 645–663. [PubMed: 2806429]

Maepea O, Bill A, 1992. Pressures in the juxtacanalicular tissue and Schlemm's canal in monkeys. Exp Eye Res 54, 879–883. [PubMed: 1521580]

Overby DR, Stamer WD, Johnson M, 2009. The changing paradigm of outflow resistance generation: towards synergistic models of the JCT and inner wall endothelium. Exp Eye Res 88, 656–670. [PubMed: 19103197]

Quigley HA, 1995. Number of people with glaucoma worldwide. Br J Ophthalmol 80, 389–393.

Raviola G, Raviola E, 1981. Paracellular route of aqueous outflow in the trabecular meshwork and canal of Schlemm: a freeze-fracture study of the endothelial junctions in the sclerocorneal angle of the macaque monkey eye. Invest Ophthalmol Vis Sci 21, 52–72. [PubMed: 7251302]

Scott PA, Lu Z, Liu Y, Gong H, 2009. Relationships between increased aqueous outflow facility during washout with the changes in hydrodynamic pattern and morphology in bovine aqueous outflow pathways. Exp Eye Res 89, 942–949. [PubMed: 19679123]

Segawa K, 1973. Pore structures of the endothelial cells of the aqueous outflow pathway: Scanning electron microscopy. Jpn J Ophthalmol 17, 133–139.

Tripathi RC, 1971. Mechanism of the aqueous outflow across trabecular wall of Schlemm's canal. Exp Eye Res 11, 116–121. [PubMed: 4108660]

Tripathi RC, 1972. Aqueous outflow pathway in normal and glaucomatous eyes. Br J Ophthalmol 56, 157–174. [PubMed: 4113454]

Vahabikashi A, Gelman A, Dong B, Gong L, Cha EDK, Schimmel M, Tamm ER, Perkumas K, Stamer WD, Sun C, Zhang HF, Gong H, Johnson M, 2019. Increased stiffness and flow resistance of the inner wall of Schlemm's canal in glaucomatous human eyes. Proc Natl Acad Sci U S A, 1–9.

Vranka JA, Bradley JM, Yang YF, Keller KE, Acott TS, 2015. Mapping molecular differences and extracellular matrix gene expression in segmental outflow pathways of the human ocular trabecular meshwork. PLoS One 10, e0122483. [PubMed: 25826404]

Vranka JA, Staverosky JA, Reddy AP, Wilmarth PA, David LL, Acott TS, Russell P, Raghunathan VK, 2018. Biomechanical Rigidity and Quantitative Proteomics Analysis of Segmental Regions of the Trabecular Meshwork at Physiologic and Elevated Pressures. Invest Ophthalmol Vis Sci 59, 246–259. [PubMed: 29340639]

Yang CY, Liu Y, Lu Z, Ren R, Gong H, 2013. Effects of Y27632 on aqueous humor outflow facility with changes in hydrodynamic pattern and morphology in human eyes. Invest Ophthalmol Vis Sci 54, 5859–5870. [PubMed: 23920374]

Zhou EH, Krishnan R, Stamer WD, Perkumas KM, Rajendran K, Nabhan JF, Lu Q, Fredberg JJ, Johnson M, 2012. Mechanical responsiveness of the endothelial cell of Schlemm's canal: scope, variability and its potential role in controlling aqueous humour outflow. J R Soc Interface 9, 1144–1155. [PubMed: 22171066]

HIGHLIGHTS

- Serial block-face scanning electron microscopy study of Schlemm's canal endothelium

- More giant vacuoles with both I-pores and basal openings found in high-flow areas

- Giant vacuoles with I-pores were larger in size than those without I-pores

- Larger size and thinner cellular lining of giant vacuoles associated with I-pores
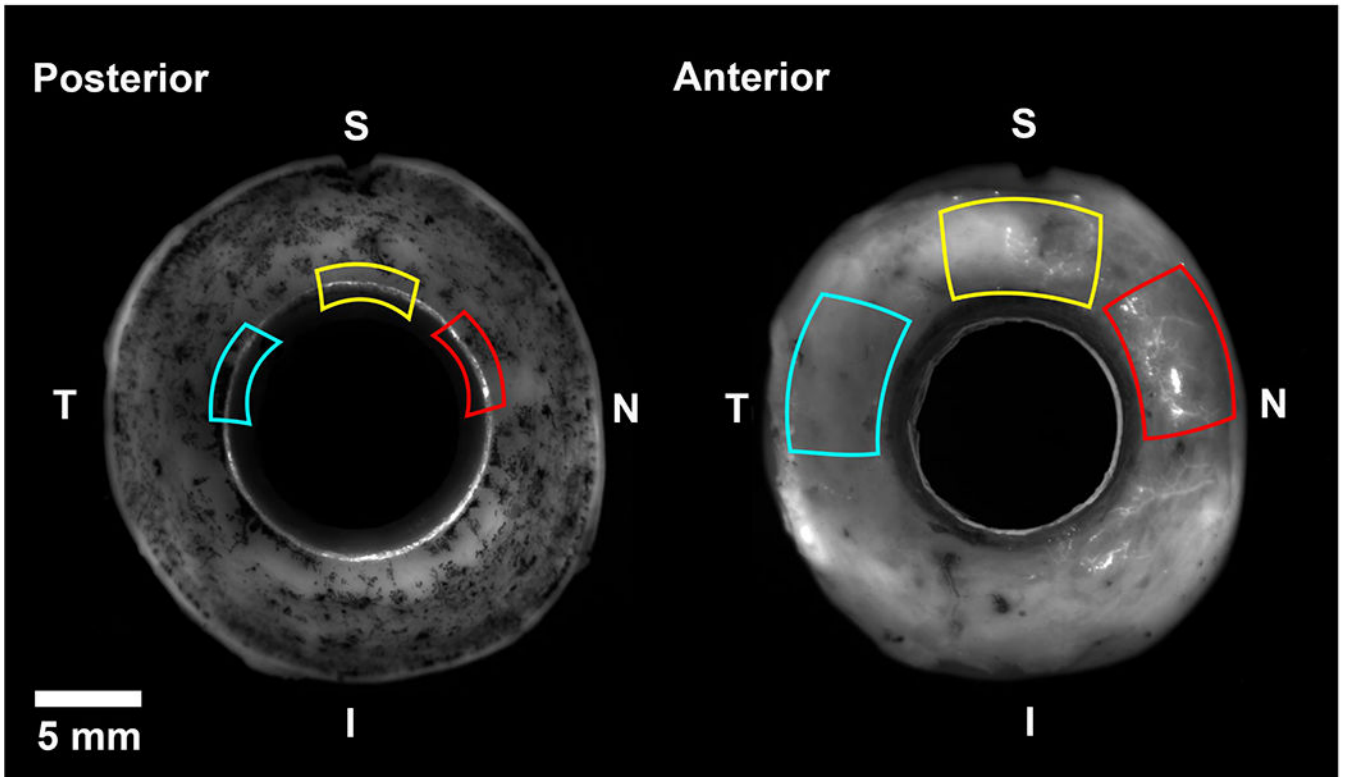
Figure 1. Global imaging of fluorescent tracer distribution in three flow-type areas
Using fluorescent tracer distribution patterns from global imaging, flow-type areas were dissected for serial block-face scanning electron microscopy. High-flow area (*red*) had bright fluorescence on both the posterior (trabecular meshwork) and anterior (episcleral veins) sides. Low-flow areas (*yellow*) had intermediate fluorescence on both sides. Non-flow areas (*blue*) had no visible fluorescence on either side. I = inferior; N = nasal; S = superior; T = temporal.
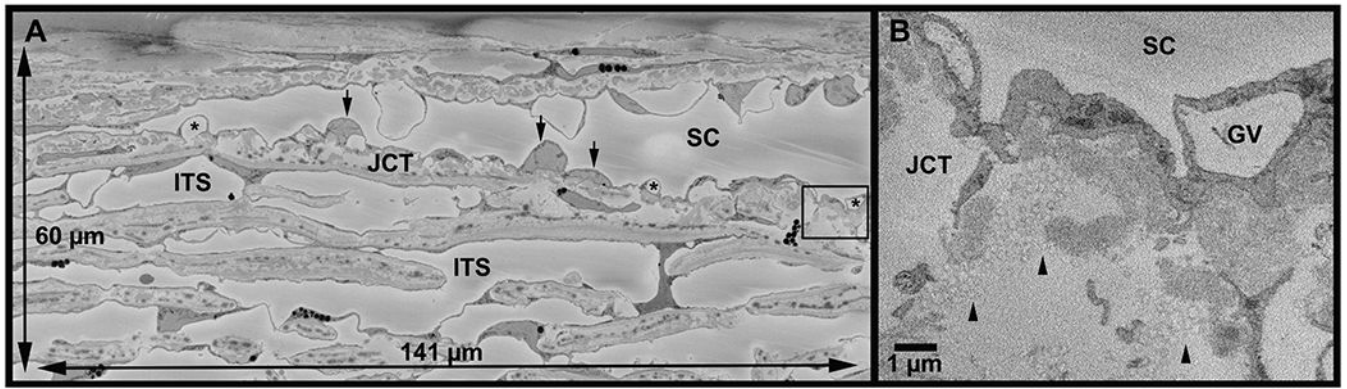
Figure 2. Full imaging field and tracer visualization on serial block-face scanning electron micrograph

A: An example of the full imaging field (141 μm x 60 μm) from a high-flow area of Eye 2. Schlemm's canal (SC) is visible with inner wall cell nuclei (*arrows*) and their giant vacuoles (*). The area in *box* is shown at higher magnification in **B**. ITS = intertrabecular space; JCT = juxtacanalicular connective tissue. **B:** Inset of area shown in *box* in **A**. Tracers (*arrowheads*) are identifiable as circles with a maximum diameter of 200 nm. GV = giant vacuole.
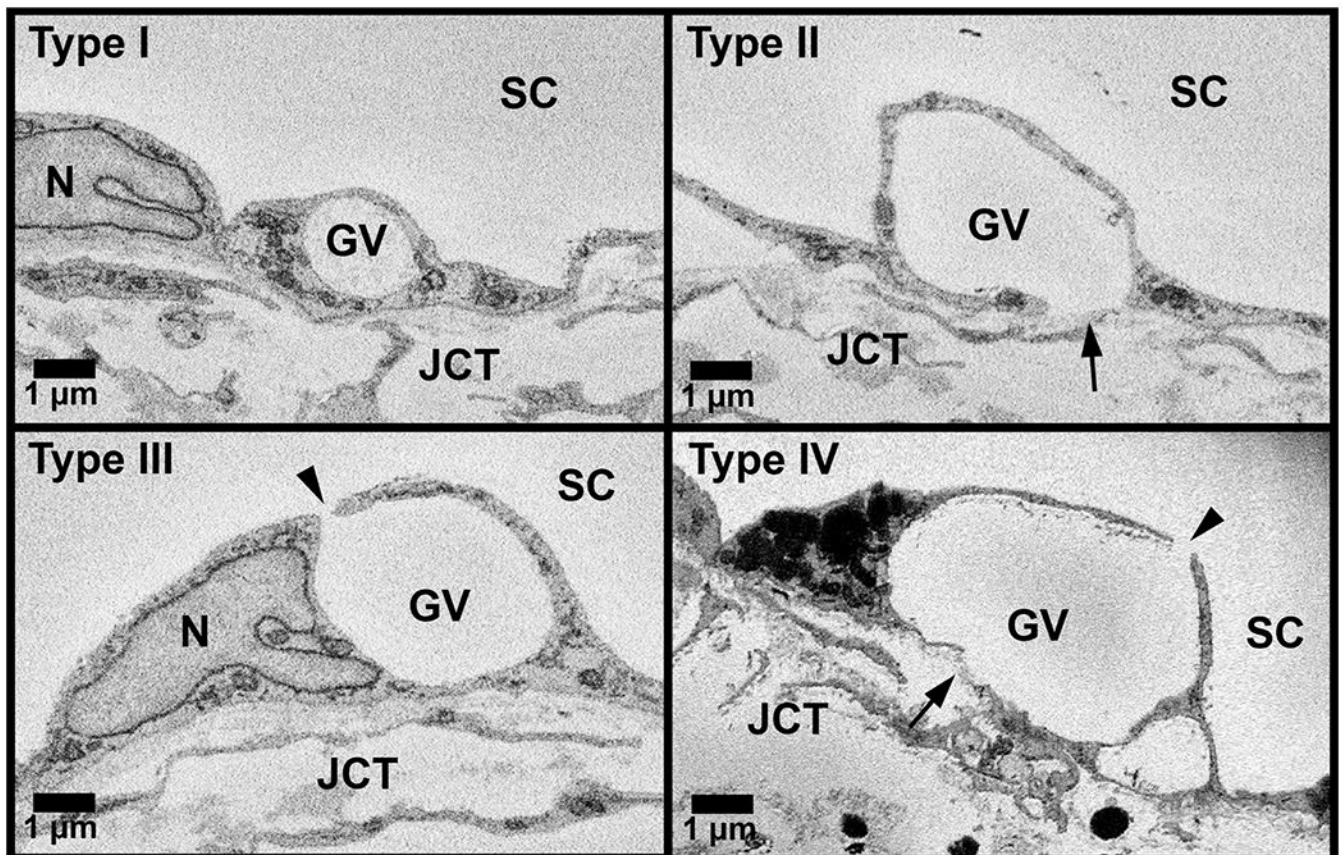
Figure 3. Four types of giant vacuoles

All GVs that were completely within the imaging field ($n = 3,302$) were categorized into the following four types based on basal openings and luminal I-pores: **Type I:** giant vacuole (GV) without either basal opening or luminal I-pore; **Type II:** GV with only basal opening (*arrow*); **Type III:** GV with only luminal I-pore (*arrowhead*); and **Type IV:** GV with both luminal I-pore and basal opening. JCT = juxtacanalicular connective tissue; SC = Schlemm's canal; N = inner wall endothelial cell nucleus.
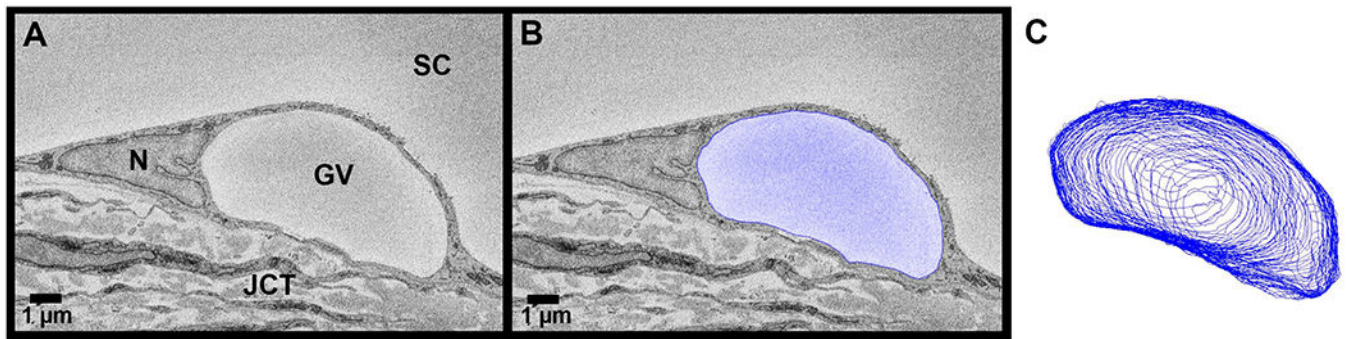
Figure 4. Giant vacuole 3D-reconstruction from serial block-face scanning electron micrographs
Giant vacuoles (GVs) were identified throughout each block (**A**) of serial electron micrographs. A subset of all GVs ($n = 180$) were traced (*blue*) (**B**) to reconstruct their geometries in 3-dimensions (**C**) and to calculate their volumes and surface areas. JCT = juxtacanalicular connective tissue; SC = Schlemm's canal; N = inner wall endothelial cell nucleus.
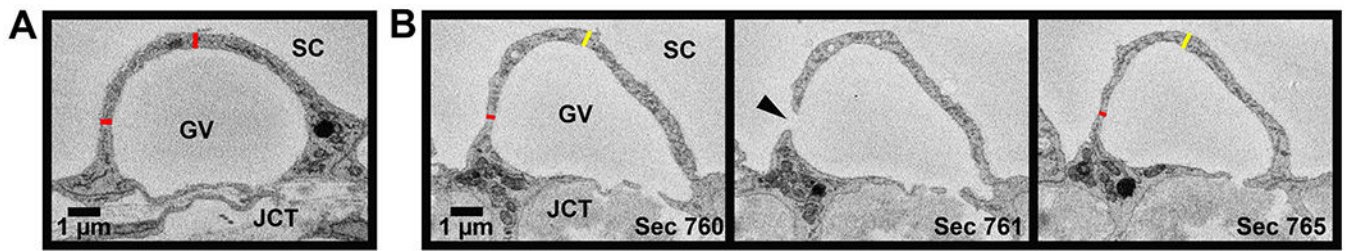
Figure 5. Methods for measurement of thickness of cellular lining of the giant vacuoles
For all 180 3D-reconstructed giant vacuoles (GVs), the thickness of the cellular lining of the GVs was measured in two ways. **A:** Thickness of cellular lining of a GV (*red*) measured on top of the GV and 90° to the side on the largest cross-sectional area section and sections away from the largest area. **B:** Peri-pore measurement (*red*) of thickness of cellular lining of a GV measured on the section before and after I-pore (*arrowhead*). Away measurement (*yellow*) taken on same sections 90° away from peri-pore measurement. JCT = juxtacanalicular connective tissue. SC = Schlemm's canal.
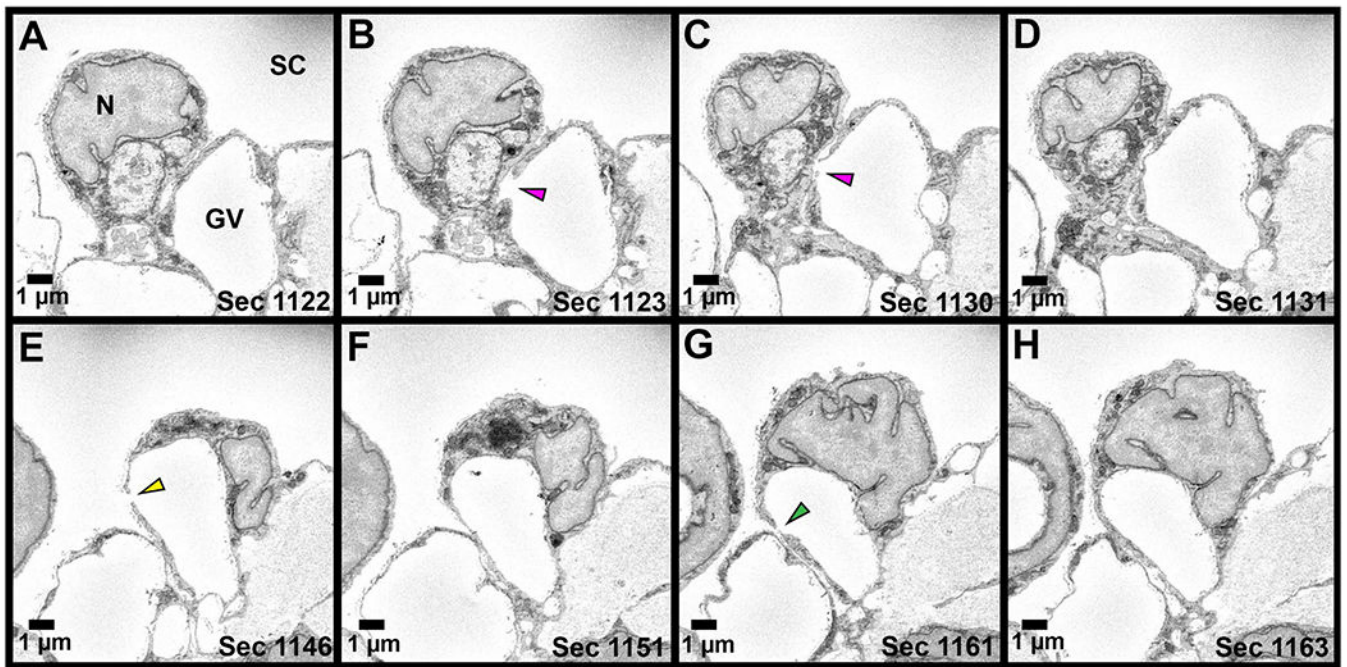
Figure 6. Serial electron micrographs through a giant vacuole (GV) with three pores
Series of electron micrographs through a GV with three I-pores is shown. **A:** Section before the I-Pore 1 is observed. **B-C:** I-Pore 1 (*pink arrowhead*) spans 8 sections. **D:** I- Pore 1 has closed. **E:** I-Pore 2 (*yellow arrowhead*) appears sixteen sections after Pore 1 and spans 2 sections. **F:** I-Pore 2 has closed. **G:** I-Pore 3 (*green arrowhead*) appears fourteen sections after I-Pore 2 and spans two sections. All three I-pores appear on the same side of the GV. N = inner wall endothelial cell nucleus; SC = Schlemm's canal.
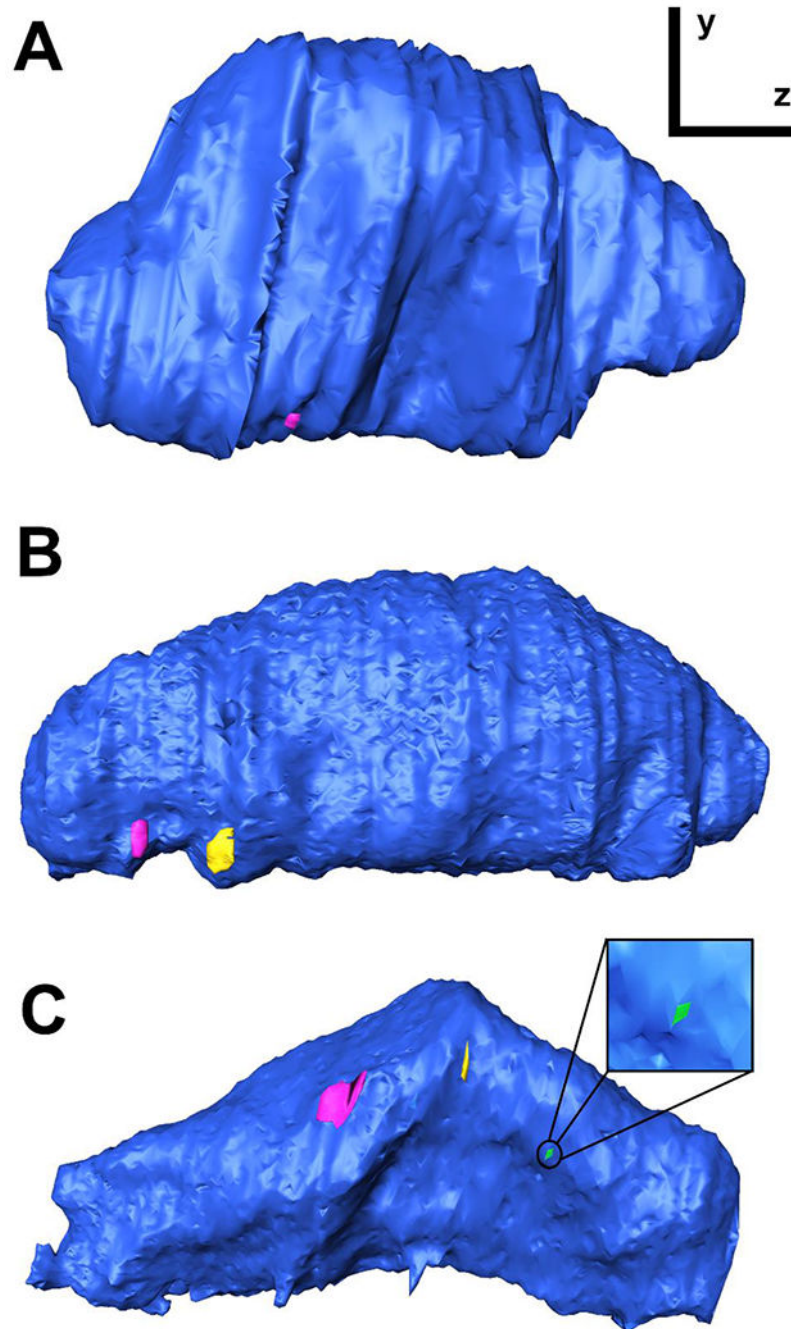
Figure 7. 3D-reconstructions of giant vacuoles with a single I-pore or multiple I-pores
Side-view of 3D reconstructions of GVs (*blue*) with one I-pore (**A**), two I-pores (**B**), and three I-pores (**C**). The GV reconstructed in (**C**) is the same GV shown in Figure 6. I-pores shown in *pink, yellow,* and *green (inset in C]*.
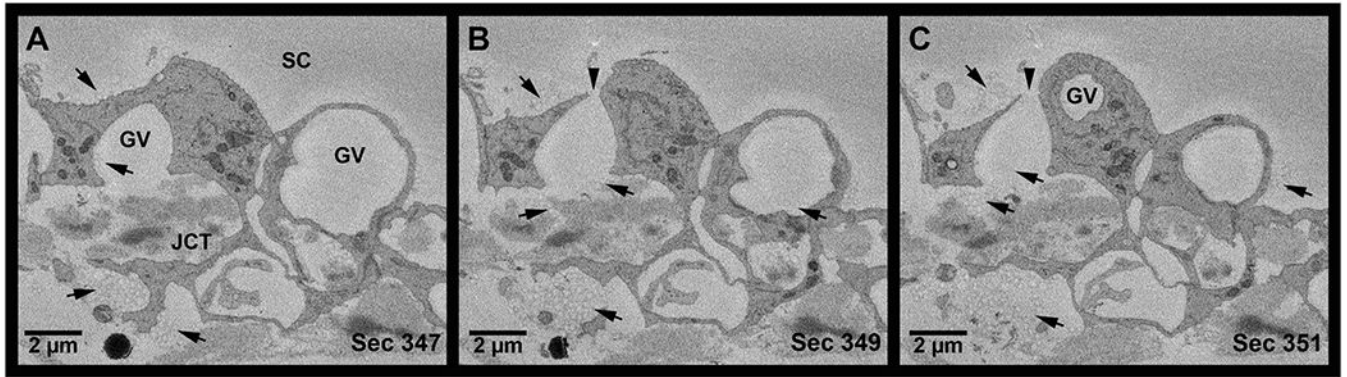
Figure 8. Serial electron micrographs showing tracers in pathway from juxtacanalicular connective tissue through a Type IV giant vacuole to Schlemm's canal in high-flow area
A: Tracers (*arrows*) were observed in the juxtacanalicular connective tissue (JCT), inside a Type IV giant vacuole (GV), and above the GV in the lumen of Schlemm's canal (SC) in high-flow area. **B:** Tracers were observed near the basal opening of a Type IV GV and in the lumen of Schlemm's canal near the luminal I-pore (*arrowhead*). Tracers were also observed inside an adjacent GV. **C:** Tracers observed entering the GV from the JCT. Additional tracers were observed in the lumen of SC.
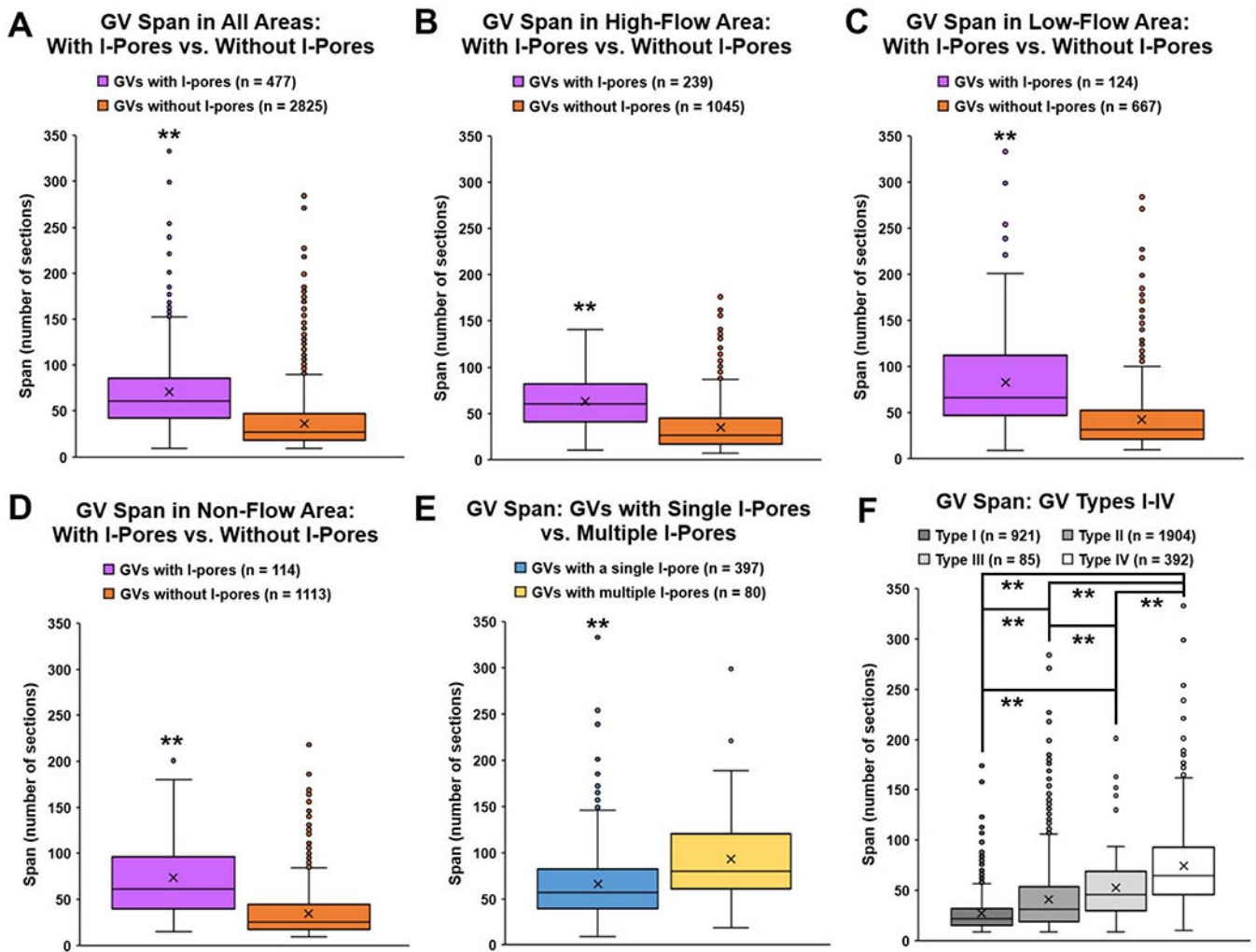
Figure 9. Span of giant vacuoles

Number of sections (span) in which each giant vacuole (GV) ($n = 3302$) appears was counted for each GV fully within the imaging field. **A:** Median span of GVs with I-pores (61 sections, IQR: 42 – 86) was significantly larger than GVs without I-pores (27, IQR: 18 – 47; P 0.01). **B:** In high-flow areas, median span of GVs with I-pores (60, IQR: 41 – 82) was significantly larger than GVs without I-pores (26, IQR: 17 – 45; P 0.01). **C:** In low-flow areas, median span of GVs with I-pores (66, IQR: 47 – 112) was significantly larger than GVs without I-pores (32, IQR: 21 – 53; P 0.01). **D:** In non-flow areas, median span of GVs with I-pores (62, IQR: 40 – 96) was significantly larger than GVs without I-pores (25, IQR: 17 – 44; P 0.01). **E:** Median span of GVs with multiple I-pores (80, IQR: 61 – 120) was significantly larger than GVs with a single I-pore (57, IQR: 39 – 82; P 0.01). **F:** The median span of Type I GVs was 22 sections (IQR: 15 – 32). Median span of Type II GVs was 31 sections (IQR: 19 – 54), and this was significantly larger than Type I (P 0.01). Median span of Type III GVs was 46 sections (IQR: 30 – 69), which was significantly larger than Type I and II (both P 0.01). Median span of Type IV GVs was 65 sections (IQR: 46 – 93), which was significantly larger than all other types (all P 0.01). **Type I:** no basal

opening or I-pore; **Type II:** basal opening, no I-pore; **Type III:** with I-pore, no basal opening; **Type IV:** both basal opening and I-pore. **P 0.01
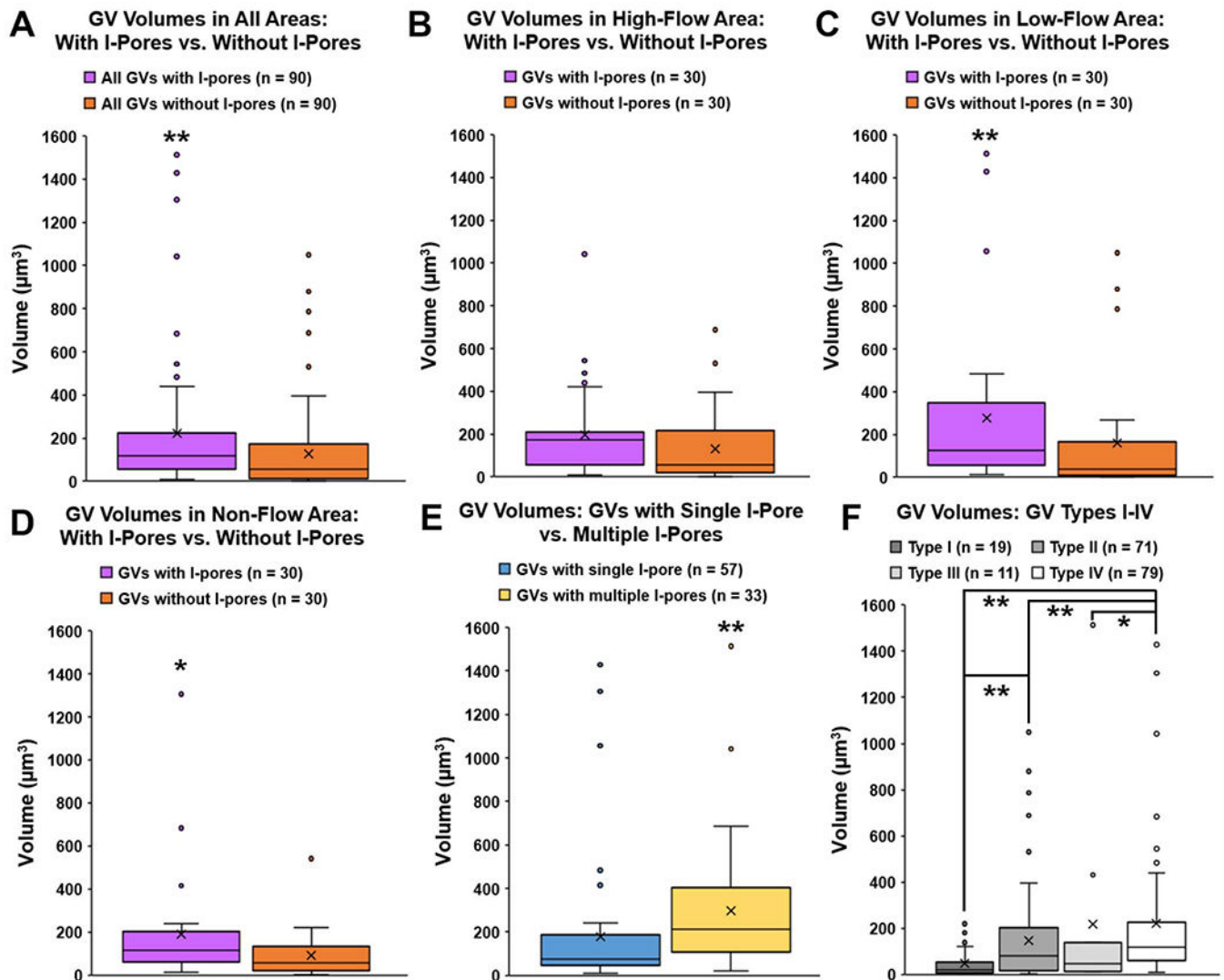
Figure 10. Volumes of 180 3D-reconstructed giant vacuoles

A: Overall, median volume of GVs with I-pores (116.93 μm^3, IQR: 56.66 – 224.10) was significantly larger than median volume of GVs without I-pores (54.82 μm^3, IQR: 12.40 – 164.46; P 0.01). **B:** In high-flow areas, the median volume of GVs with I-pores (172.39 μm^3, IQR: 56.82 – 209.30) was not quite significantly larger than the median volume of GVs without I-pores (55.12 μm^3, IQR: 19.06 – 217.29; P = 0.07). **C:** In low-flow areas, median volume of GVs with I-pores (127.00 μm^3, IQR: 56.40 – 348.56) was significantly larger than those without I-pores (37.57 μm^3, IQR: 10.39 – 167.24; P = 0.01). **D:** In non-flow areas, median volume of GVs with I-pores (113.91 μm^3, IQR: 61.82 – 201.22) was significantly larger than those without I-pores (58.34 μm^3, IQR: 20.78 – 132.73; P = 0.03). **E:** Median volume of GVs with multiple I-pores (212.59 μm^3, IQR: 114.19 – 401.50) was significantly larger compared to the median volume of GVs with a single I-pore (75.80 μm^3, IQR: 45.78 – 186.84; P 0.01). **F:** Median volumes of four types of GVs varied significantly (P 0.01). Specifically, Type II (with basal opening, no I-pore) median volume (79.65 μm^3, IQR: 19.13 – 202.88) was significantly larger than Type I (no basal opening or I-pore) median volume

(20.78 μm^3, IQR: 6.90 – 51.15; P = 0.01). Type IV GVs (with both basal opening and I-pore) median volume (119.72 μm^3, IQR: 61.83 – 225.81) was significantly larger than Types I, II, and III (P 0.01 to Types I, II; P = 0.03 to Type III). *Whiskers*: 1.5 interquartile range (IQR). X = mean. *P < 0.05; **P 0.01.
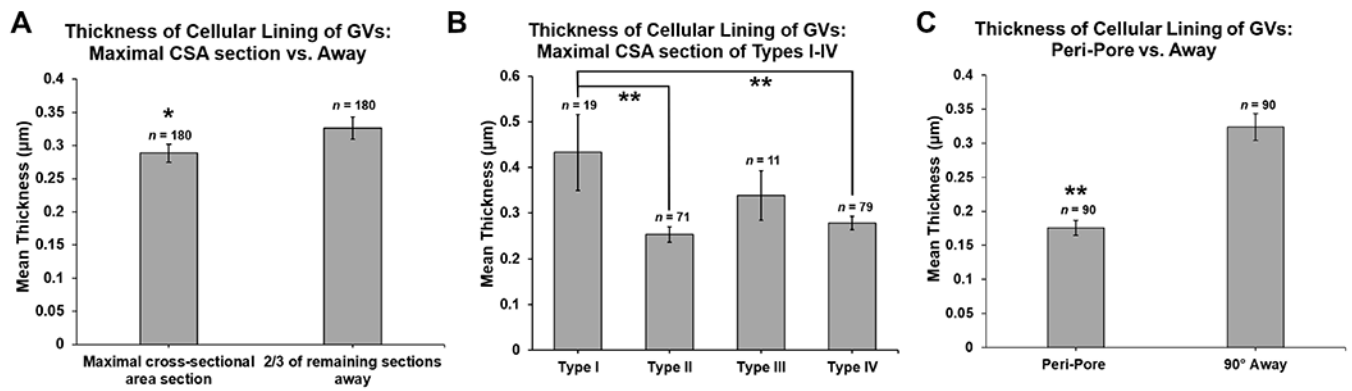
Figure 11. Thickness of the cellular lining of the 180 3D-reconstructed GVs

A: Mean thickness of the cellular lining of the GVs was significantly thinner on sections with maximal cross-sectional area (CSA) of GVs than those sections away from the maximal CSA (mean of # of sections away: 22, range: 3-146, based on size of each GV) (P = 0.03). **B:** Mean thickness of the cellular lining of GV types measured on the section with maximal CSA. Mean thickness was significantly thinner in GV Types II (basal opening, no I-pore) and IV (both basal opening and I-pore), compared to Type I GVs (no basal opening or I-pore) (both P 0.01). **C:** Mean thickness of the cellular lining of the GVs in the peri-pore region on the section before and after an I-pore was significantly thinner than 90° away from the I-pore area on the same sections (P 0.01). *Error bars*: SEM. *$P < 0.05$; **P 0.01.
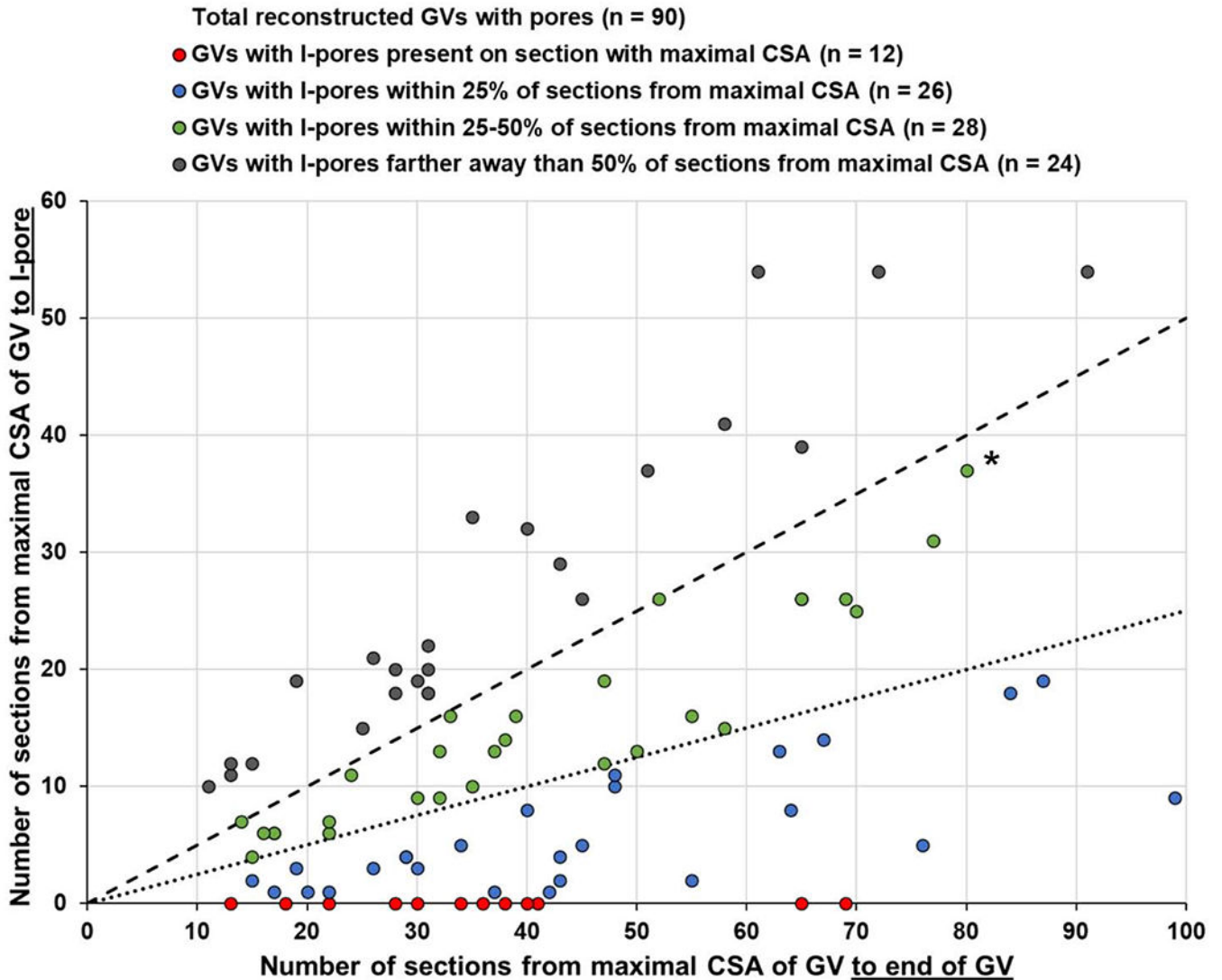
Figure 12. Proximity of I-pores to the sections of the GVs with the largest cross-sectional area (CSA)

Proximity of I-pores to maximal CSA of GV was determined as a proportion of the number of sections from maximal CSA to I-pore / number of sections from maximal CSA to end of GV. For example, the *starred green point* shows that I-pore was 37 sections away from the maximal CSA, and there were 80 sections to the end of the GV, so this I-pore was within 46.2% (37/80) of sections from maximal CSA to end of GV. 12/90 (13.3%) of I-pores were present in the section with the maximal CSA of the GV (*red points*). 38/90 (42.2%) of I-pores were present either in the section with the maximal CSA or within 25% of sections from the maximal CSA (points on graph fall below the 25% *dotted line* including *red* and *blue points*). 66/90 (73.3%) of I-pores were present within 50% of sections from maximal CSA (points on graph fall below the 50% *dashed line* including *green, blue,* and *red points*).

24/90 (26.7%) of I-pores were farther away than 50% of sections from the maximal CSA (*gray points* above the 50% *dashed line*).

Table 1.

Summary of observed I-pores and endothelial cell nuclei over entire surface area of inner wall in three flow-type areas

Flow-Type Area	Eye	Number of Images	I-Pore Count[†]	Nuclei Count	Inner Wall Surface Area (mm²)
High-flow	1	1380	186	149	0.025
	2	1800	106	52	0.024
	Total	**3180**	**292**	**201**	**0.049**
Low-flow	1	1493	95	121	0.026
	2	2181	55	59	0.040
	Total	**3674**	**150**	**180**	**0.065**
Non-flow	1	1578	55	74	0.027
	2	1370	85	88	0.025
	Total	**2948**	**140**	**162**	**0.052**
Overall Total		**9802**	**582**	**543**	**0.166**

[†] I-pores were only counted if associated with a giant vacuole.

Table 2.

Counts of giant vacuoles observed and percentage of GVs with pores

Flow-Type Area	Eye	Count: GVs observed over entire surface area[†]	Count: GVs within imaging field[‡]	Count: GVs with I-pores[‡]	Percentage GVs with I-pores[#]
High-flow	1	1023	975	151	15.5%
	2	317	309	88	28.5%
	Total	**1340**	**1284**	**239**	**18.6%**
Low-flow	1	608	579	83	14.3%
	2	217	212	41	19.3%
	Total	**825**	**791**	**124**	**15.7%**
Non-flow	1	424	396	43	10.9%
	2	861	831	71	8.5%
	Total	**1285**	**1227**	**114**	**9.3%**
Overall		**3450**	**3302**	**477**	**14.4%**

[†]These values include giant vacuoles (GVs) that were partially outside the imaging field on the left-hand side or the beginning of the block but exclude those on the right-hand side and end of block.

[‡]These values only include GVs that were completely within the imaging field.

[#]Percentages were calculated by dividing counts of GVs with I-pores by GVs within imaging field.

Table 3.

Counts of GV types by flow-type areas for all GVs

Flow-Type Area	Eye	Type I (%)	Type II (%)	Type III (%)	Type IV (%)	Total[†]
High-flow	1	250 (25.6%)	574 (58.9%)	32 (3.3%)	119 (12.2%)	975
	2	50 (16.2%)	171 (55.3%)	5 (1.6%)	83 (26.9%)	309
	Total	**300 (23.4%)**	**745 (58.0%)**	**37 (2.9%)**	**202 (15.7%)**	**1284**
Low-flow	1	167 (28.8%)	329 (56.8%)	21 (3.6%)	62 (10.7%)	579
	2	44 (20.8%)	127 (59.9%)	3 (1.4%)	38 (17.9%)	212
	Total	**211 (26.7%)**	**456 (57.6%)**	**24 (3.0%)**	**100 (12.6%)**	**791**
Non-flow	1	105 (26.5%)	248 (62.6%)	11 (2.8%)	32 (8.1%)	396
	2	305 (36.7%)	455 (54.8%)	13 (1.6%)	58 (7.0%)	831
	Total	**410 (33.4%)**	**703 (57.3%)**	**24 (2.0%)**	**90 (7.3%)**	**1227**
Overall		**921 (27.9%)**	**1904 (57.7%)**	**85 (2.6%)**	**392 (11.9%)**	**3302**

Type I: no basal opening or luminal I-pore; **Type II**: basal opening, no luminal I-pore; **Type III**: luminal I-pore, no basal opening; **Type IV**: both basal opening and luminal I-pore.

[†] total numbers of GVs that were completely within the imaging field.

Table 4.

Densities of giant vacuoles with I-pores in three flow-type areas

Flow-Type Area	Eye	Density: GVs / IW nucleus[†]	Density: GVs / IW Area (/mm²) [†]	Density: GVs with I-pores/IW nucleus[‡]	Density: GVs with I-pores/IW Area (/mm²) [‡]
High-flow	1	6.87	40269	1.06	6236
	2	6.10	12976	1.74	3696
Low-flow	1	5.02	23774	0.72	3408
	2	3.70	5467	0.71	1057
Non-flow	1	5.72	15876	0.62	1724
	2	9.77	34150	0.83	2918

[†] These values were calculated by dividing counts of GVs observed over entire surface area as listed in Table 2 by the number of nuclei or IW surface area as listed in Table 1.

[‡] These values were calculated by dividing counts of GVs with I-pores as listed in Table 2 by the number of nuclei or IW surface area as listed in Table 1.